

Temperature and Entropy Fields of Baryonic Gas in the Universe

Ping He^{1,2}, Long-Long Feng^{1,3}, and Li-Zhi Fang²

ABSTRACT

The temperature (T) and entropy (S) fields of baryonic gas, or intergalactic medium (IGM), in the Λ CDM cosmology are analyzed using simulation samples produced by a hybrid cosmological hydrodynamic/ N -body code, effective capturing shocks and complex structures with high precision. We show that in the nonlinear regime the dynamical similarity between the IGM and dark matter will be broken in the presence of strong shocks in the IGM. The heating and entropy production by the shocks breaks the IGM into multiple phases. There are no single-value relations between T or S and the mass densities of the IGM (ρ_{igm}) or dark matter (ρ_{dm}). The probability distribution functions of the temperature and entropy fields are long-tailed, with a power law decreasing on the sides of high temperature or high entropy. These fields are therefore intermittent. The mean entropy, or the cosmological entropy floor, is found to be more than $100 h^{-1/3}$ keV cm² in all regions when $z \leq 1$. At redshift $z \simeq 2 - 3$, high-entropy gas ($S > 50 h^{-1/3}$ keV cm²) mostly resides in areas on scales larger than $1 h^{-1}$ Mpc and with density $\rho_{dm} > 10^2$ (in units of $\bar{\rho}_{dm}$). Therefore, gravitational shocks are an effective preheating mechanism of the IGM and probably enough to provide the entropy excess of clusters and groups if the epoch of the gas falling in cluster cores is not earlier than $z \simeq 2 - 3$. On the other hand, at redshifts $z \leq 4$, there is always a more than 90% volume of the low dark matter mass density ($\rho_{dm} \leq 2$) regions filled by the IGM with temperature less than $10^{4.5}$ K. Therefore, the multiphased character and non-Gaussianity of the IGM field would explain the high-temperature and high-entropy gas observed in groups and clusters with low-temperature IGM observed by Ly α forest lines and the intermittency observed by the spikes of quasi-stellar object's absorption spectrum.

Subject headings: cosmology: theory - intergalactic medium - large-scale structure of the universe - methods: numerical

¹National Astronomical Observatories, Chinese Academy of Sciences, 20A Datun Road, Chaoyang, Beijing 100012, China

²Department of Physics, University of Arizona, Tucson, AZ 85721

³Purple Mountain Observatory, Chinese Academy of Sciences, Nanjing, 210008

1. Introduction

The standard scenario that provides the theoretical skeleton for the formation of cosmic large-scale structures in the universe is the hierarchical clustering scenario. This scenario assumes that massive dark matter halos are formed via the processes of gravitational collapse, merging of smaller structures, and accretion. Light-emitting and -absorbing objects form when the baryonic gas, i.e., the intergalactic medium (IGM), falls, cools, and condenses around and within the dark halos. The evolution of the IGM in this model is largely determined by the underlying dark matter. It is usually assumed that the dynamical behavior of the IGM field can be obtained from the dark matter field by a similarity mapping between the two (e.g., Kaiser 1986). The perturbations in the density and velocity distribution of the IGM are considered to be the same as those of the dark matter field point by point on scales larger than the Jeans length scales.

In the linear regime, this similarity mapping is correct. Even when the perturbations of the initial IGM distribution are different from those of the dark matter, linear growth modes will lead to similarity on scales larger than the Jeans length (Bi et al. 1992; Fang et al. 1993; Nusser 2000; Nusser & Haehnelt 1999). However, in the nonlinear regime, the similarity between the IGM and dark matter fields on scales larger than the Jeans length may not always be present. It has been shown in hydrodynamics that a passive component generally decouples from the underlying field during nonlinear evolution (for a review, see Shraiman & Siggia 2000). For instance, a passive component might be highly non-Gaussian, even when the underlying field is Gaussian (Kraichnan 1994). This nonlinear decoupling is common in stochastic systems consisting of a “passive component” in an underlying mass field.

In the system consisting of the IGM and dark matter, the IGM can be considered a “passive component”, because the evolution of the IGM is driven by the gravity of the underlying dark matter. Moreover, the system of the IGM and dark matter is stochastic because of the randomness of the initial perturbations of the cosmic mass and velocity fields. The mass and velocity fields of the IGM and dark matter are random variables. The importance of the stochastic nature in the evolution of cosmic mass and velocity fields has been emphasized in many works (e.g., Berera & Fang 1994; Jones 1999; Buchert et al. 1999; Matarrese & Mohayee 2002; Coles & Spencer 2003; Ma & Bertschinger 2004). Therefore, in the nonlinear regime, we expect that the similarity mapping between the IGM and the dark matter may no longer work.

The dynamical mechanism of violating the similarity between the IGM and dark matter has been discussed in the early study of structure formation (Shandarin & Zel'dovich 1989). As the dark matter particles are collisionless, the velocity of the dark matter particles will be

multivalued at the intersection of the dark matter particle trajectories. On the other hand the IGM, being an ideal fluid, has a single-value velocity field. Thus, at the intersection of the dark matter particle trajectories, the density of gas would be discontinuous, and shocks or complex structures occur. The development of shocks or complex structures breaks the similarity between the IGM and dark matter and thus leads to the statistical discrepancy between the IGM distribution and dark matter mass field.

Strong shocks and complex structures result in the heating and the entropy increase of the IGM. The cosmic baryonic gas involved in strong shocks should hence undergo an entropy increase. The dark matter remains unaffected. Consequently, the IGM will be in thermodynamically multiple phases. The relations between the temperature and mass density, or entropy and mass density of the IGM will not be described by an single-value relation and will vary from place to place. It would be interesting to study the multiphased properties of the IGM caused by the statistical discrepancy between the fields of the IGM and dark matter. In this paper, we focus on the temperature and entropy fields of the IGM.

Aside from theoretical interests, this study is also motivated by the problem of the so-called entropy excess, i.e., a high entropy floor is observed in nearby groups and low-mass clusters (Ponman et al. 1999; Lloyd-Davies et al. 2000). Entropy excess indicates that some processes that violate the dynamical self-similar scaling are important in structure formation. To explain this result, many models for IGM preheating have been proposed, such as photoionization heating (e.g., Efstathiou 1992; Gnedin 2000), supernova (SN) explosions, active galactic nucleus (AGN) activities (e.g., Cole et al. 1994; Somerville & Primack 1999), gravitational shocks associated with clusters (Cavaliere et al. 1998) or warm-hot gas (Valageas et al. 2003).

The decoupling of the IGM and dark matter in the nonlinear regime inevitably leads to a dynamical break of the similarity between dark matter and gas. Hence, the temperature and entropy fields of the IGM formed by this evolution should be treated as the background or cosmological “floor”. The entropies produced by other mechanisms are superpositions on this background. Many previous studies assumed an uniform heating of the IGM all over the space (e.g., Mo & Mao 2002). However, this assumption will not hold if the background temperature and entropy are inhomogeneous and multiphased. Some studies of the gravitational shock heating have assumed that the heating and entropy increase occur only in nearby groups and clusters. This is to assume that shock heating occurs mainly in high-density regions. However, the decoupling evolution and gravitational shocks can happen in high mass density regions (hosting groups and clusters), as well as in low mass density areas. Thus, shocks can also heat the IGM at low mass density areas.

The last motivation for this study is the progress made in the art of numerical algorithms

for hydrodynamics over the last few years. The weighted essentially nonoscillatory (WENO) scheme (Fedkiw et al. 2003; Shu 2003) has proved to be significantly superior over the piecewise smooth solution algorithm containing discontinuities. It has been successful in capturing shocks and complex structures and in calculating the entropy in both shocked and unshocked regions. Therefore, it would be interesting to calculate the temperature and entropy fields of the IGM with this code.

We analyze the temperature and entropy fields of the IGM in the Λ CDM cosmology with simulation samples produced by a hybrid hydrodynamic/ N -body code. This code effectively simulates shocks and complex structures with high precision. The paper is arranged as follows. The basic equations and the mechanism of the IGM-dark matter discrepancy are addressed in §2. In §3 we present the hydrodynamic cosmological simulation scheme. In §4 we show the basic properties of the temperature field of the IGM. The entropy field of the IGM is calculated and analyzed in §5. Finally, in §6 we present our conclusions followed by a discussion of the results.

2. The basic equations

2.1. Hydrodynamic equations for the IGM

The IGM is assumed to be an ideal fluid with polytropic index γ . The hydrodynamic equations for the IGM in the expanding universe can be written as

$$\dot{U} + \partial_i f^i(U) = f(t, U) \quad (1)$$

where $\partial_i \equiv \partial/\partial X^i$ ($i = 1, 2, 3$); X^i denote the proper coordinates, which are related to comoving coordinates x^i by $X^i = a(t)x^i$, $a(t)$ being the scale factor. The quantity U in equation(1) contains five components:

$$U = (\rho, p, \mathbf{v}, E) \quad (2)$$

where ρ is the comoving density of the IGM, $\mathbf{v} = \{v_i\}$ is the peculiar velocity, $E = P/(\gamma - 1) + \frac{1}{2}\rho\mathbf{v}^2$ is the total energy per unit comoving volume, $P = a^3 p$, and p is the pressure of the IGM. The quantities $f^i(U)$ in equation(1) are given by the conservation laws of mass, momentum, and energy as

$$\begin{aligned} f^1(U) &= [\rho v^1, \rho(v^1)^2 + P, \rho v^1 v^2, \rho v^1 v^3, v^1(E + P)] \\ f^2(U) &= [\rho v^2, \rho v^1 v^2, \rho(v^2)^2 + P, \rho v^2 v^3, v^2(E + P)] \\ f^3(U) &= [\rho v^3, \rho v^1 v^3, \rho v^2 v^3, \rho(v^3)^2 + P, v^3(E + P)] \end{aligned} \quad (3)$$

The “force” term $f(t, U)$ on the right-hand side of equation(1) is given by

$$f(t, U) = (0, -\frac{\dot{a}}{a}\rho\mathbf{v} + \rho\mathbf{g}, -2\frac{\dot{a}}{a}E + \rho\mathbf{v} \cdot \mathbf{g} - \Lambda_{rad}). \quad (4)$$

The term of $-(\dot{a}/a)\rho\mathbf{v}$ is from the expansion of the universe. The term of Λ_{rad} in equation (4) is given by the radiative heating-cooling of the baryonic gas. The gravitational force $\mathbf{g} = -\nabla\phi$ is produced by the collisionless dark matter, given by

$$\nabla^2\phi = 4\pi G a^2 \bar{\rho}_{tot} \delta_{tot}, \quad (5)$$

where the operator ∇ acts on the comoving coordinate \mathbf{x} ; $\delta_{tot} = [\rho_{tot}(\mathbf{x}, t) - \bar{\rho}_{tot}]/\bar{\rho}_{tot}$, and ρ_{tot} is a sum of the comoving baryon and dark matter mass density. The total mean density is $\bar{\rho}_{tot}(t) = 1/6\pi G t^2 \propto a^{-3}$. The gravitational potential ϕ is zero (or constant) when the density perturbation $\delta_{tot} = 0$.

2.2. The statistical discrepancy between the IGM and dark matter

Before embarking on the numerical calculations, we point out some qualitative features of the IGM evolution given by equation (1). To sketch the evolution of gravitational clustering, we ignore the heating and cooling. Consider the case in which all thermal processes are described by the polytropic relations $p(\mathbf{x}, t) \propto \rho^\gamma(\mathbf{x}, t)$, $T \propto \rho^{\gamma-1}$, or $T = T_0(1 + \delta)^{\gamma-1}$, where $\delta = [\rho(\mathbf{x}, t) - \bar{\rho}]/\bar{\rho}$ is the IGM mass density perturbation. From equation (1), the momentum equation is

$$\frac{\partial a\mathbf{v}}{\partial t} + (\mathbf{v} \cdot \nabla)\mathbf{v} = -\frac{\gamma k_B T}{\mu m_p} \frac{\nabla\delta}{(1 + \delta)} - \nabla\phi \quad (6)$$

where the parameter μ is the mean molecular weight of the IGM particles and m_p is the proton mass.

For growth modes in the perturbations, velocity is irrotational. We can then define a velocity potential by

$$\mathbf{v} = -\frac{1}{a}\nabla\varphi. \quad (7)$$

In the linear approximation of the temperature-dependent term, equation (6) yields

$$\frac{\partial\varphi}{\partial t} - \frac{1}{2a^2}(\nabla\varphi)^2 - \frac{\nu}{a^2}\nabla^2\varphi = \phi, \quad (8)$$

where the coefficient ν is given by

$$\nu = \frac{\gamma k_B T_0}{\mu m_p (d \ln D(t)/dt)}, \quad (9)$$

in which $D(t)$ describes the linear growth behavior. The term with ν in equation (8) acts like a viscosity (due to thermal diffusion) characterized by the Jeans length $k_J^2 = (a^2/t^2)(\nu m_p/\gamma k_B T_0)$.

Since the gravitational potential ϕ is mainly given by the random density field of dark matter, the term ϕ of equation (8) plays the role of a random force. The nonlinear equation (8) is exactly the stochastic force-driven Burgers equation or the Kardar-Parisi-Zhang (KPZ) equation (Kardar et al. 1986; Berera & Fang 1994; Barabási & Stanley 1995). The behavior of the field φ given by equation (8) depends on the Reynolds number, defined by $\mathcal{R} \equiv (r_c/a_0)^{4/3}$ (e.g., Lässig 2000), where r_c is the comoving correlation length of the random field ϕ and a_0 is the dissipation length. In the case of equation (8), the dissipation length is given by the Jeans smoothing equation (9), or $a_0 = \nu^{3/4} r_c^{1/2} \langle \phi^2 \rangle^{-1/4} (d \ln D/dt)^{-1/4}$. Thus, we have

$$\mathcal{R} = (k_J r_c)^{2/3} \left(\frac{k_J}{k} \right)^{4/3} \langle \delta_{dm}^2(k) \rangle^{1/3}, \quad (10)$$

where $\delta_{dm}(k)$ is the Fourier component of the dark matter density contrast for the wavenumber k . To derive equation (10), we assume that the gravitational potential ϕ is only given by the dark matter mass perturbation.

It is well known that the Burgers equation does not reduce, but increase initial chaos (Kraichnan 1968). When the Reynolds number (eq. [10]) is larger than 1, the φ field is in Burgers turbulence (e.g., Lässig 2000). That is, when the Reynolds number is high, an initially random field always results in a collection of shocks with a smooth and simple variation of the field between the shocks.

The correlation length r_c of the gravitational potential ϕ is larger than the Jeans length, i.e., $k_J r_c > 1$. Therefore, \mathcal{R} can be larger than 1 on scales larger than the Jeans length ($k < k_J$), even when $\delta_{dm}(k_J)$ is of the order of 1. This means that the Burgers turbulence on scales larger than the Jeans length can occur in the IGM φ field, when the dark matter mass density perturbations are still quasi-linear or weakly nonlinear ($\delta_{dm}(k) \simeq 1$) on those scales. This results in the decoupling of IGM velocity field from that of the dark matter on scales larger than the Jeans length. When the Burgers turbulence develops in the IGM, the field φ is characterized by strong intermittency and contains many discontinuities, or shocks. The probability distribution function (PDF) of φ is long-tailed (Lässig 2000). That is, the randomly distributed shocks and intermittent spikes lead to the statistical discrepancy between the velocity fields of the IGM and dark matter.

3. Cosmological hydrodynamic simulations

3.1. Method of hydrodynamical simulations

From the result of §2, it is clear that we need to focus on shocks and discontinuities in our simulations. In the system of the IGM gravitationally coupled with dark matter, the temperature of the IGM generally is in the range $10^4 - 10^6$ K, and the speed of sound in the IGM is only a few km s^{-1} to a few tens km s^{-1} . On the other hand, the rms bulk velocity of the IGM is of the order of hundreds km s^{-1} (Zhan & Fang 2002). Hence, the Mach number of the gas can be as high as ~ 100 (Ryu et al 2003). The shocks and discontinuities are extremely strong. Hence we will not use a Lagrangian approach such as the smoothed particle hydrodynamic (SPH) algorithm. A main challenge to the SPH scheme is the handling of shocks or discontinuities, because the nature of SPH is to smooth the fields considered (e.g. Borve et al. 2001; Omang et al. 2003.)

We take a Eulerian approach instead. A well-known problem of the Eulerian algorithm are the unphysical oscillations near a discontinuity. An effective method to reduce the spurious oscillations is given by designed limiters, such as the Total-Variation Diminishing (TVD) method (Harten 1983) and piecewise parabolic method (PPM; Collella & Woodward 1984). A problem of the TVD method is that the accuracy necessarily degenerates to first order near smooth extrema (Godlewski & Raviart 1996). This problem will cause errors in calculating the temperature and entropy changes because they are determined by the difference of the thermal energy $P/(\gamma - 1)$ on the two sides of the shock. When the Mach number of gas is high, the thermal energy $P/(\gamma - 1)$ is very small compared to the kinetic energy $\rho\mathbf{v}^2/2$. To overcome this problem, the essentially nonoscillatory (ENO) and WENO algorithms were proposed (Harten et al. 1986; Shu 1998, 2003; Fedkiw et al. 2003). They can simultaneously provide a high-order precision for both the smooth part of the solution and sharp shock transition (Liu et al. 1994; Jiang & Shu 1996).

The WENO scheme WENO has been successfully applied to hydrodynamic problems containing shocks and complex structures, such as shock-vortex interaction (Grasso & Pirozzoli 2000a, 2000b), interacting blast waves (Liang & Chen 1999; Balsara & Shu 2000), Rayleigh-Taylor instability (Shi et al. 2003), and MHD (Jiang & Wu 1999). WENO has also been used to study astrophysical hydrodynamics, including stellar atmospheres (Del Zanna et al. 1998), high Reynolds number compressible flows with supernova (Zhang et al. 2003), and high Mach number astrophysical jets (Carrillo et al. 2003). In the context of cosmological applications, WENO has proved especially adept at handling the Burgers equation (Shu 1999). Recently, a hybrid hydrodynamic/ N -body code based on the WENO scheme has been developed. It has passed typical tests, including the Sedov blast wave and the for-

mation of the Zel'dovich pancake (Feng et al. 2004). This code has been successfully used to produce the quasi-stellar object (QSO) Ly α transmitted flux, including the high-resolution sample HP1700+6416 (Feng et al. 2003). The statistical features of these samples are in good agreement with observed features not only on second-order measures, like the power spectrum, but also up to orders as high as 8 for the intermittent behavior. Hence, we believe that it would be reasonable to study the entropy and temperature fields of the IGM with the simulation samples given by the WENO scheme.

3.2. Samples

For the purpose of this paper, we run the hybrid N -body/hydrodynamic code to trace the cosmic evolution of the coupled system of both dark matter and baryonic gas in a flat low-density Λ CDM model, which is specified by the cosmological parameters $(\Omega_m, \Omega_\Lambda, h, \sigma_8, \Omega_b) = (0.3, 0.7, 0.7, 0.9, 0.026)$. The baryon fraction is fixed using the constraint from primordial nucleosynthesis as $\Omega_b = 0.0125h^{-2}$ (Walker et al. 1991). The linear power spectrum is taken from the fitting formulae presented by Eisenstein & Hu (1998).

The simulations were performed in a periodic, cubic box of size $25 h^{-1}\text{Mpc}$ with a 192^3 grid and an equal number of dark matter particles. The simulations start at a redshift $z = 49$, and the results are noted at the redshifts of $z = 4.0, 3.0, 2.0, 1.0, 0.5$, and 0.0 . The time step is chosen by the minimum value among the following three timescales. The first is from the Courant condition given by

$$\delta t \leq \frac{cfl \times a(t)\Delta x}{\max(|v_x| + c_s, |v_y| + c_s, |v_z| + c_s)} \quad (11)$$

where Δx is the cell size, c_s is the local sound speed, v_x, v_y and v_z are the local fluid velocities, and cfl is the Courant number, for which we take $cfl = 0.6$. The second timescale is imposed by cosmic expansion, which requires that $\Delta a/a < 0.02$ within a single time step. The last timescale comes from the requirement that a particle moves not more than a fixed fraction of the cell size.

We then produced two realizations. One includes the radiative cooling and heating, and one does not. For the latter, the initial temperature of gas is taken to be 10^4 K. For the former, the atomic processes, including ionization, radiative cooling, and heating, are modeled in the same way as in Cen (1992) in a plasma of hydrogen and helium of primordial composition ($X = 0.76, Y = 0.24$). The processes such as star formation, feedback due to SNs, and AGN activities have not yet been taken into account. A uniform UV background of ionizing photons is assumed to have a power-law spectrum of the form $J(\nu) = J_{21} \times 10^{-21}(\nu/\nu_{HI})^{-\alpha}\text{erg}$

$\text{s}^{-1}\text{cm}^{-2}\text{sr}^{-1}\text{Hz}^{-1}$, where the photoionizing flux is normalized by the parameter J_{21} at the Lyman limit frequency ν_{HI} and is suddenly switched on at $z > 10$ to heat the gas and reionize the universe.

For statistical studies, we randomly sampled 500 one-dimensional (1D) fields from the simulation results at every redshift of $z=4, 3, 2, 1, 0.5$, and 0.0. Each one-dimensional sample, of size $L=25 \text{ h}^{-1}\text{Mpc}$, contains 192 data points. For each of these points, information about the mass density and peculiar velocity of dark matter, and mass density, peculiar velocity, and temperature of the IGM are recorded. All of the statistical analyses below are based on the first realization, i.e., the one including cooling and heating. The second one is only used to produce Figure 9, which shows the effects of cooling and heating.

3.3. An example of the IGM field

We select one sample as an example of the IGM field and show in Figure 1 the one-dimensional spatial distributions of the temperature, mass density, and peculiar velocity of the IGM at the two redshifts $z=0$ and $z=0.5$. For comparison, we also show the densities and velocities of dark matter in the corresponding panels. For identification, we use the notations ρ_{dm} and ρ_{igm} for the mass densities of the dark matter and IGM, respectively (ρ in §2 actually is ρ_{igm} .) The mass densities ρ_{dm} and ρ_{igm} are in units of $\bar{\rho}_{dm}$ and $\bar{\rho}_{igm}$, which are the mean densities of dark matter and gas, respectively. Spatial position is described by the comoving coordinate x .

Figure 1 shows clearly that the relations between the density and velocity fields of the dark matter and IGM are very complex. The density and velocity fields of the IGM are not always faithful tracers of the underlying dark matter fields, although in the linear regime they are point-by-point tracers on scales larger than the Jeans length (Bi et al. 1992; Fang et al. 1993; Bi 1993; Nusser 2000; Matarrese & Mohayaee 2002). Many of the discrepancies between the IGM and dark matter fields shown in Figure 1 can be explained by the Jeans smoothing (Theuns et al. 2000). However, Figure 1 shows that several differences between the mass fields of the IGM and dark matter are on scales of a few $\text{h}^{-1} \text{ Mpc}$, which is larger than the corresponding Jeans length of the IGM.

The big jump in the IGM temperature around the position $x \simeq 13 \text{ h}^{-1} \text{ Mpc}$ is typically caused by a strong shock. The temperature of the preshocked gas is $\sim 10^3 \text{ K}$ and increases to 10^6 K by the shock. In this case, the temperature increases by a factor of $\sim 10^3$. According to the shock theory of a polytropic gas (Landau & Lifshitz 1959), the Mach number should be $M \simeq \sqrt{10^3} \simeq 30$. The value is reasonable. Moreover, for strong shocks, the density has

to increase by a factor of $\sim (\gamma + 1)/(\gamma - 1) = 4$. This is also consistent with the density field shown in Figure 1. It is also interesting to note that the jump exists in the region of $\rho_{dm} < 1$, i.e., not located close to filaments of dark matter. Therefore, gravitational shocks of the IGM can develop not only around massive dark halos but also in low-density regions.

4. Temperature field of the IGM

4.1. Multiple phases in the temperature-density diagram

In Figure 2 we show the relations between the temperature and mass density of the IGM at $z = 4, 3, 2, 1, 0.5$, and 0.0 . Each panel in Figure 2 contains 19,200 data points randomly drawn from a total of 500 samples at each redshift. The basic feature of the $T - \rho_{igm}$ diagram looks similar to those given by other cosmological hydrodynamic simulations or semi-analytical models (e.g., Ryu et al. 1993; Katz et al. 1996; Theuns et al. 1998; Davé et al. 1999; Valageas et al. 2002; Springel & Hernquist 2002). Roughly speaking, there are two phases in the $T - \rho_{igm}$ plane. (1) The first phase manifests a tight correlation in the bottom left regions T ($\leq 10^{4.5}$ K) and $0.01 < \rho_{igm} < 2$, and (2) the second phase lies above the tight correlation regions and has a scattered distribution in which the temperature generally is greater than 10^5 K.

The tight correlation lines can be well approximated by a power law as $T \propto \rho_{igm}^\alpha$ with α slightly increasing from ~ 0.61 at $z=4$ to ~ 0.69 at $z=0$, which is the same as the so-called IGM equation of state given by Hui & Gnedin (1997). The small discrepancy of α from the adiabatic index $\gamma - 1 = 2/3$ results from the photoionization heating and radiative cooling (Valageas et al. 2002).

The gas in phase 2 sometimes is called the warm-hot intergalactic medium (WHIM), as its temperature is $\sim 10^5 - 10^7$ K, i.e., higher than the gas in phase 1 by a factor of about $10 - 10^3$ (Cen & Ostriker 1999). From Figure 2 we can see that the WHIM underwent a significant evolution from redshift $z = 4$ to the present. At $z = 4$ WHIM events are rare and mostly reside in the regions of mass density, $\rho_{igm} \geq 1$, while WHIM becomes quite common when $z \leq 2$. Note that the high-temperature ($10^6 - 10^7$ K) events, and hence strong shocks, can also occur in the regions with density $\rho_{igm} \sim 1$, and even $\rho_{igm} \simeq 0.1$. In other words, the case shown in Figure 1 is common.

Comparing with numerical results cited above by other groups, phase 2 gas is more significant in our simulation. Especially in the low mass density ($\rho_{igm} < 1$) regions, the phase 2 in Figure 2 is pronounced. This is because the WENO code is more effective in capturing shocks in both high- and low-density regions.

4.2. Statistical decoupling between the IGM and dark matter

From Figure 1 we have already seen the discrepancy between the IGM and dark matter fields. The ρ_{igm}/ρ_{dm} ratios are not equal to unity everywhere. Hence, the baryonic fraction is not always equal to the cosmological average value $f_b = \Omega_b/\Omega_m = 0.085$. To show this deviation, we plot the relationships between the mean baryonic fraction and temperature in Figure 3. It is obvious that the baryon fraction at $z \leq 1$ significantly exceeds the cosmological value f_b for the WHIM (at $10^5 \text{ K} < T < 10^7 \text{ K}$). This is a well-known result nowadays (Cen & Ostriker 1999; Davé et al. 2001). The concentration of baryons into WHIM can be seen as follows. The gas is compressed by a factor of ~ 4 by strong shocks. On the other hand, the dark matter mass density at the pre- and postshock is almost the same. Thus, the baryon fraction in the postshocked IGM can be enhanced as high as $4 \times 0.085 \simeq 0.3$. This result is consistent with what is shown in Figure 3.

However, WHIM may not necessarily reside in dense regions. In Figure 4 we present a cumulative probability distribution $P(> \rho_{dm})$ for WHIM ($T > 10^5 \text{ K}$) at different redshifts, which is the fraction of WHIM with dark matter density larger than ρ_{dm} . Note that we use the dark matter density ρ_{dm} in Figure 4, not ρ_{igm} , as massive dark halos should be identified by high ρ_{dm} , rather than by high ρ_{igm} . If gravitational collapsing or collapsed regions are characterized by $\rho_{dm} > 10$, Figure 4 shows that most of WHIM at $z \leq 2$ does not reside in or close to massive dark halos. In other words, many strong shocks may not be due to the accretion by the filaments of dark matter. One should not simply identify all WHIM as dense clouds or massive halos.

4.3. Probability Distribution Functions of temperature field

The multiphased features of the temperature field can be described by the PDF of the temperature field. The results are shown in Figure 5. We use three density ranges: (1) low, $0.1 < \rho_{dm} < 0.4$, (2) medium, $0.4 < \rho_{dm} < 2.0$, and (3) high, $2 < \rho_{dm} < 10$. All PDFs have similar shape but shift to higher temperature with higher density. The PDFs are sharply peaked at some low temperatures, while some have long tails on the high-temperature side. The tails are approximately given by a power law T^{-a} with the index $a \simeq 4$ at $z = 4$, and $a \simeq 1.7$ at $z = 0$. Therefore, the high-temperature tails are prolonged at low redshifts. A field with such power-law-tailed PDF is typically intermittent (Nakao 1998). We also calculate the $T - \rho_{dm}$ diagram, which shows the similar result of multiphased structure as the $T - \rho_{igm}$ diagram.

We show in Figure 6 the relations between the mean temperature \bar{T} and the dark matter

mass density ρ_{dm} . One can see that \bar{T} is actually inadequate to describe the temperature field if the field is long-tailed, or multiphased. From Figure 6 we can see that \bar{T} at redshifts ≤ 1 and $\bar{\rho}_{dm} \sim 1$ is in the range $10^4.5 - 10^5$ K. However, Figure 5 shows that in the range $\bar{\rho}_{dm} \sim 1$ the probability for temperature of $10^3 - 10^4$ K is comparable to the probability for $T = 10^4 - 10^5$ K. Therefore, the IGM cannot be approximately modeled as a single phase gas with temperature of either $\sim 10^4.5 - 10^5$ K or $10^3 - 10^4$ K.

In Figure 6 each panel has three $\bar{T} - \rho_{dm}$ curves, which correspond to the data smoothed by windows on scales 0.26, 1.04 and 4.17 $\text{h}^{-1} \text{Mpc}$, respectively. It is interesting to see that the $\bar{T} - \rho_{dm}$ relations are basically independent of the smoothing scales. Therefore, the multiphased feature of the IGM temperature does not come from the sampling, but from the non-Gaussian PDF of the field. Such a field is substantially different from a uniform or a Gaussian field.

The $\bar{T} - \rho_{dm}$ relation of WHIM given by Davé et al. (2001) is approximately $\bar{T} \propto \rho_{igm}$. From Figure 6 we can also see $\bar{T} \propto \rho_{igm}$. However, they are different. The mean \bar{T} in Figure 6 is given by averaging over all pixels including both the WHIM and the gas with low ($< 10^5$ K) temperature, since the $\bar{T} - \rho_{dm}$ relation for low ($< 10^5$ K) temperatures is $\bar{T} \propto \rho_{igm}^a$ with $a < 1$. Therefore, for WHIM only, we may have $\bar{T} \propto \rho_{igm}^a$ and $a > 1$. Therefore, Figure 6 shows again that our samples contain more shock-heated events.

5. Entropy field of the IGM

5.1. Entropy-temperature and entropy-mass density relations

The entropy of the IGM is measured by the parameter $T/n_{igm}^{2/3}$, where n_{igm} is the number density of baryons. It is actually related to the entropy density s of the IGM by $s/\rho_{igm} = \ln T/n_{igm}^{2/3} + \text{const}$. As we will not use s below, we use this notation for the entropy parameter or simply entropy, $S = T/n_{igm}^{2/3}$. If temperature T is in units of keV ($1 \text{ keV} \simeq 1.2 \times 10^7$ K), entropy S is in units of keV cm². Figure 7 presents the relation between the entropy and temperature of the IGM at $z = 4, 3, 2, 1, 0.5$, and 0 for the 19,200 data randomly drawn from the total 192^3 data points.

Figure 7 also shows the two phases of the IGM: (1) a tight correlation along a line of $S \simeq \text{const}$ at the bottom of the figure, i.e., the entropy of the IGM is independent of IGM temperature, and (2) a scattered distribution above the tight correlation line. They are the same as Figure 2. The gas in phase 1 approximately satisfies $T \propto \rho_{igm}^{2/3}$. The gas in phase 2 experiences an entropy increase process, mainly because of the heating by shocks and complex structures in the IGM. A strong shock increases T by a factor of $10^1 - 10^3$,

n_{igm} by a factor of ~ 4 , and therefore, the postshocked entropy can be enhanced by a factor of $10^1 - 10^3$.

Phase 2 shows a significant evolution from redshift $z = 4$ to the present. There are almost no high-entropy ($S > 50 h^{-1/3}$ keV cm 2) events when $z = 4$. At $z = 2$ and 3, high-entropy events are biased to $T > 5 \times 10^{-3}$ keV regions. When $z \leq 1$, high-entropy events occur in all temperatures $T > 10^{-3}$ keV, or greater than 10^4 K ranges.

The S - ρ_{dm} diagram is shown in Figure 8. We again use ρ_{dm} , not ρ_{igm} , as the clustering of the mass field is indicated by high- ρ_{dm} . Although ρ_{igm} does not trace ρ_{dm} point by point, one can still see the two phases: a dense distribution along a line of constant S , and a scattered distribution above the line, given by the entropy increase because of shocks. For redshift $z < 3$, the gas in phase 2 can reside in both low ($\rho_{dm} < 1$) and high ($\rho_{dm} > 1$) dark matter density areas.

Figure 9a presents the mean entropy \bar{S} versus density ρ_{dm} . The entropy of the IGM increases by about 2 orders of magnitude from redshift $z = 4$ to 0.5. In the redshift range $3 > z > 1$, the mean entropy \bar{S} is higher in higher density areas. For dark matter mass density $\rho_{dm} > 10^2$, the mean entropy \bar{S} is greater than $60 h^{-1/3}$ keV cm 2 at the epoch $z \simeq 2$, and greater than $20 h^{-1/3}$ keV cm 2 at $z \simeq 3$. At $z \leq 0.5$, the shocks and complicated structures yield an “entropy floor” $\bar{S} \sim 100 - 300 h^{-1/3}$ keV cm 2 at $z \leq 0.5$ over the entire IGM from low-density ($\rho_{dm} \simeq 10^{-2}$) areas to high-density ($\rho_{dm} \simeq 10^3$) regions. This is the cosmological background of entropy floor generated by the nonlinear evolution of the IGM in the gravity of dark matter.

In Figure 9b we show the \bar{S} - ρ_{igm} relation for samples produced by the same cosmological parameters, but without considering radiative cooling and photoionization heating. We see that the relation \bar{S} - ρ_{igm} at $z \leq 2$ in Figure 9b is about the same as that of Figure 9a. Especially in the high-density range ($\rho_{dm} > 10$), Figures 9a and 9b are the same. Therefore, the entropy increase of the IGM at $z \leq 2$ shown in Figure 9a is not due to the heating and cooling, but mainly determined by shocks and complicated structures. The effects of radiative cooling and heating to the entropy evolution are negligible at $z \leq 2$ and high-density areas. At higher redshift $z > 2$ and low-density areas, however, the effects of radiative cooling and heating become important.

It is interesting to compare our result of the entropy floor with the semi-analytical estimation by Valageas et al. (2003, hereafter VSS03). Using the data of Davé et al (2001), they found that WHIM can provide an entropy floor (or the mean \bar{S}) of the order of $10^2 h^{-1/3}$ keV cm 2 at $z \leq 0.5$, which is about the same as Figure 9. However, their result is given by an average of S over all WHIM. As has been pointed out in §3.2, most WHIM at $z \leq 2$ does

not reside in high-density areas. Therefore, it is unclear whether the high-entropy floor given by an overall average of the WHIM is in the high-density areas. Moreover, the average of S in VSS03 is done by the method of adiabatically bringing all patches into a same effective density. With this method, the low-density areas would have significant contribution to the mean S . In our study, the mean of S is taken in each given bin of the dark matter density, and therefore from Figure 9 one can unambiguously conclude that the high-entropy floor of $\sim 10^2 h^{-1/3}$ keV cm 2 first formed in high-density $\rho_{dm} > 10$ areas since $z = 2$, i.e., the areas that are favored by the formation of galaxy clusters.

Moreover, the mean of S given by VSS03 falls steeply with redshift. VSS03 found $\bar{S} < 10 h^{-1/3}$ keV cm 2 at $z \geq 1.5$. Figure 9 also shows the decrease of \bar{S} with redshift. However, it is much slower than that of the VSS03. Figure 9 shows that the entropy floor is still $\bar{S} > 10 h^{-1/3}$ keV cm 2 when $z = 3$ and $\rho_{dm} > 10$. The difference between the redshift dependence of the VSS03 and Figure 9 is caused by two reasons. (1) The number of \bar{S} of the VSS03 is given by an average over all density regions, and Figure 9 shows that the decrease of \bar{S} with redshift is faster in lower density ($\rho_{dm} < 1$) regions; and (2) the WENO code is more effective in describing shocks than the data used in VSS03.

5.2. PDF of entropy field

At first glance, the mean entropy of Figure 9 may contradict the Ly α absorption in QSO's absorption spectrum. A uniform entropy floor $S \sim 100 h^{-1/3}$ keV cm 2 corresponds to $T \simeq 1.8 \times 10^5$ K at $z = 1$ and $\rho_{igm} \simeq 1$. This temperature is obviously unacceptable with the observations of Ly α forest lines. Even for a uniform entropy floor as small as $10 h^{-1/3}$ keV cm 2 , the IGM temperature is about 4×10^4 K at $z = 2$ and $\rho_{igm} \simeq 1$. This is also contradictory with the small-scale intermittent spikes in the transmitted flux of QSO's Ly α absorption. This argument is often used to constrain preheating models. However, this argument no longer holds if the IGM is multiphased. This can be seen from the PDF of the entropy field.

Similar to the temperature field, the entropy field is also highly non-Gaussian. Figure 10 presents the PDFs of the entropy field at redshifts from $z = 4$ to 0. The shapes of the PDFs at different redshifts are similar, but the curves shift to higher S at lower z . The PDFs are peaked at the low-entropy end and gradually decrease with the increasing S by a power law $\propto S^{-b}$ with $b \simeq 4$ at $z \sim 4$ and $b \simeq 1.6$ at $z \sim 0$. That is, the tail is longer when the redshift z decreases. Therefore, in terms of entropy, the IGM is also in multiple phases. High- and low-entropy gas coexist in the IGM. In this case, the mean entropy, \bar{S} , does not mean uniform heating. For a long-tailed PDF, the mean is much larger than the median.

Thus, most of the space actually has entropy S less than the mean.

Figure 11 gives the volume filling factor $V(> S)$, which is the volume fraction with entropy larger than a given S . It shows that the volume fraction of high entropy ($S > 100h^{-1/3}$ keV cm 2) is very small for all redshifts. Although the mean entropy \bar{S} is as high as $\sim 200h^{-1/3}$ keV cm 2 at $z = 0$ (Figure 9a), the volume fraction $V(> 200)$ is only about 10%. Therefore, it is not surprising that the high- and low-entropy phases can coexist in the IGM. To approximate such a multiphased field by a uniform distribution would be misleading.

5.3. Mass fraction of high-entropy and high-density regions

We now study the distribution of entropy of the IGM in mass space. We are interested in the regions with high entropy and high density, as they provide the environment of baryonic structure formation. Let us consider the regions with high dark matter density $\rho_{dm} = 5$ or 10 to be the hosts of collapsed baryonic clumps. Figure 12 shows the baryonic mass fraction $M(> S)$ of regions with the entropy larger than a given S and dark matter density $\rho_{dm} > 5$ and > 10 , respectively.

First, we see from Figure 12 that $M(> 10) \simeq M(> 100)$ at $z = 0$ for either $\rho_{dm} > 5$ or > 10 . That is, at $z = 0$, no high-density regions $\rho_{dm} > 5$ have entropy less than $100 h^{-1/3}$ keV cm 2 . At higher z , the mass fraction with higher entropy becomes smaller. Nevertheless, there are already $\sim 10\%$ baryons at $z \simeq 2$ to have entropy greater than $50 h^{-1/3}$ keV cm 2 . This feature is not sensitive to whether $\rho_{dm} > 5$ or 10. Since the baryon fraction in collapsed halos is about 10%, we may conclude that all structure formation is probably in the entropy environment of $\bar{S} > 50 h^{-1/3}$ keV cm 2 if the gas falls into the halos not earlier than $z \simeq 2$.

In calculating Figure 12, the mass field ρ_{dm} was decomposed to the size of the resolution of the simulation, which is $0.13 h^{-1}$ Mpc. To study the scale dependence of the entropy floor, we decomposed the dark matter mass field and entropy field into different scales. This decomposition can be done by the orthogonal scaling functions of discrete wavelet transform (DWT). As has been showed (Xu et al. 1998), the high-density regions on the scale $1.5 h^{-1}$ Mpc given by the DWT decomposition can be identified as clusters, which yields the same result as traditional identification schemes, such as the friends-of-friends algorithm.

Figure 13 presents the relations between the mean entropy \bar{S} and ρ_{dm} for the mass field decomposed by the DWT scaling function on scales $L = 0.26, 1.04$ and $4.17 h^{-1}$ Mpc. The mean \bar{S} in Figure 13 is given by averaging over all regions that are on the given scale and have the dark matter density ρ_{dm} in a given bin. Therefore, \bar{S} at $L = 1.04 h^{-1}$ and $\rho_{dm} > 10$ is the mean entropy of the IGM in the regions that host the formation of groups and clusters.

Figure 13 also shows that the \bar{S} - ρ_{dm} relations are basically scale-independent when $z \geq 3$. At small redshifts $z \leq 2$, however, one can see that the larger the size L , the higher the mean entropy is in high-density regions. That is, the high-entropy IGM is biased to the places that have high dark matter density in a large size area. This is probably because more shocks occur around massive halos. Thus, at epochs $z \leq 2$, massive halos are generally surrounded by high-entropy baryonic gas. This result shows again that the entropy floor in the regions with high mass density and on large scales is generally larger than the estimation by an over-all average (VSS03).

6. Discussions and Conclusions

We have studied the evolution of the temperature and entropy fields of the IGM in the nonlinear regime of gravitational clustering. We have used the N -body/hydrodynamic simulation samples produced by the WENO code, which effectively describes shocks. Strong shocks can significantly change the mass density and velocity of the IGM fluid, at the same time having no effect on the dark matter field. Therefore, when the shocks emerge, the dynamical similarity between the IGM and dark matter is broken. The gravitational shocks and complex structures of the IGM can take place in nearby massive dark halos as well as in low mass density regions.

The entropy production by shocks makes the IGM multiphased. The temperature T and entropy S of the IGM are no longer related to the mass density ρ_{igm} or ρ_{dm} by a single-value relation. The IGM contains gas in both high- and low-entropy phases, or both high- and low-temperature phases. For a given ρ_{igm} or ρ_{dm} , the IGM temperature and entropy lie in very wide ranges from $\sim 10^3$ to $\sim 10^7$ K, and from ~ 1 to $\sim 10^3 h^{-1/3}$ keV cm 2 , respectively. Therefore, the temperature and entropy fields of the IGM cannot be approximately described by a randomly uniform Gaussian distribution.

We should point out that star formation and their feedback on the IGM evolution are not considered in our simulation. Roughly, there are two types of the feedbacks: (1) photoionization heating by the UV emission of stars and AGNs, and (2) injection of hot gas and energy by SN explosions or other sources of cosmic rays. The photoionization heating actually can be properly considered if the UV background is adjusted by fitting the simulation with observed mean flux decrement of QSO's Ly α absorption spectrum (Feng et al. 2003). The effect of injecting hot gas and energy by SNe is localized in massive halos. For instance, metal absorption systems (like CIV and MgII) in QSO spectra are generally associated with collapsed halos (e.g., Bi & Fang 1996). A recent Ly α observation around protoclusters (Adelberger et al. 2003) implies that AGN heating does not drastically affect

the gas in clusters. Nor does it affect the IGM in low-density areas. Therefore, these heating mechanisms are probably not strong enough to change the basic feature of the multiphased temperature and entropy field given in this paper.

The multiphased feature and non-Gaussianity of the IGM temperature and entropy fields can effectively be applied to explain the following IGM-related observations.

1. Entropy floor of groups and clusters.—For all regions on scales greater than $1 h^{-1}$ Mpc and with dark matter mass density $\rho_{dm} > 10^2$, the mean entropy \bar{S} , or entropy floor, is greater than $80 h^{-1/3}$ keV cm 2 since the epoch $z \simeq 2$ and greater than $20 h^{-1/3}$ keV cm 2 at $z \simeq 3$. Even for regions of $\rho_{dm} > 10$, the mean entropy still have $\bar{S} > 25 h^{-1/3}$ keV cm 2 at the epoch $z \simeq 2$ and $10 h^{-1/3}$ keV cm 2 at $z \simeq 3$ (Fig. 13). Therefore, gravitational shock is an important provider of high-entropy gas around massive halos, which are the hosts of clusters and groups. This result is adequate to explain the entropy excess from the observations of clusters and groups if the epoch of the gas falling in cluster cores is not earlier than $z \simeq 2 - 3$ (Ponman et al. 2003). In other words, the IGM is already significantly preheated by gravitational shocks at the epoch $z \simeq 2 - 3$, and therefore other sources of heating may not be important if the cluster core with entropy excess formed after that epoch (Kay & Bower 1999; Borgani et al 2002).

2. Ly α forest lines.—The Ly α forest lines in QSO’s absorption spectrum of $2 < z < 4$ have a column density N_{HI} of HI atoms in the range $13 < \ln N_{HI} < 14$, which corresponds to areas of $\rho_{dm} \simeq 1$ (Bi & Davidsen 1997). The thermal broadening of these lines shows that the temperature of the IGM at this density area is about $10^4 - 10^5$ K. The high-entropy floor ($S \sim 100 h^{-1/3}$ keV cm 2) will contradict the Ly α forest if the entropy field is uniform. However, the temperature and entropy fields are highly non-Gaussian and of multiple phases. The volume of the universe is actually dominated by regions of low temperature and low mass density. For all redshifts $z \leq 4$, more than 90% volume with dark matter mass density ($\rho_{dm} \leq 2$) is occupied by the IGM with temperature less than $10^{4.5}$ K (Fig. 5). This provides the room for the QSO’s Ly α forests. The mean temperature is higher for lower redshifts (Fig. 6). Therefore, the number density of the forests lines, or absorbers, is lower at lower redshifts. These properties match the constraints on the IGM from QSO’s Ly α forests. Moreover, the Ly α forests are very well modeled by the semianalytical lognormal model, which assumes that the PDF of the IGM mass density field is lognormal, and long-tailed (Bi & Davidsen 1997). This assumption basically is consistent with the long-tailed PDF of IGM temperature field (Fig. 5).

3. Intermittency of Ly α transmitted flux.—The Ly α transmitted flux of the QSO’s absorption spectrum is found to be remarkably intermittent (Jamkhedkar et al. 2002, 2003). That is, the power of the flux fluctuations concentrates in the rare spikes. The intermittent

features can be detected even on scales corresponding to thermal broadening of gas with $T \simeq 10^3 - 10^4$ K. Different from Ly α forests, the intermittency of the Ly α transmitted flux does not become weaker, but become even stronger at lower redshifts. It is impossible to explain the intermittency with single-phase IGM with temperature $\sim 10^4$ K. However, strong shocks yield many big discontinuities of the IGM temperature (Fig. 1), and therefore the power of the temperature fluctuations is also spiky. The long-tailed PDFs also reflect the intermittency of the temperature field. The lower the redshifts, the longer the tails, and therefore the intermittent features are more prominent at lower redshifts. Moreover, the IGM at density $\rho_{dm} \simeq 1$ regions contains components of $T \simeq 10^3 - 10^4$ K as well as of $T \simeq 10^4 - 10^5$ K. Therefore, the intermittency of the Ly α transmitted flux can be well fitted with these simulation samples (Pando et al. 2002; Feng et al. 2003).

All these results are in good agreement with the theoretical expectation of §2. In the nonlinear regime, the Reynolds number is larger and leads to the Burgers turbulence. Therefore, the gravitational shock in the IGM provides a unified explanation of the features of the IGM in both low- and higher density regions. It includes the departure of the IGM-dark matter similarity mapping, formation of the entropy excess groups and clusters, the temperature and entropy in the regions of Ly α forests and the intermittency of Ly α transmitted flux. The IGM-dark matter discrepancy gives a deep understanding of the nonlinear evolution of the system of the IGM plus dark matter.

We thank Professor C.-W Shu for helping to develop the cosmological hydrodynamic simulation code based on the WENO scheme. We also thank P. Jamkhedkar for help with the manuscript. P.H. is supported by a Fellowship of the World Laboratory. L.L.F. acknowledges support from the National Science Foundation of China (NSFC) and the National Key Basic Research Science Foundation. This work is partially supported by the National Natural Science Foundation of China (10025313) and the National Key Basic Research Science Foundation of China (NKBRSF G19990752).

REFERENCES

Adelberger, K.L., Steidel, C.C., Shapley, A.E., & Pettini, M. 2003, ApJ, 584, 45
Balsara, D., & Shu, C.-W. 2000, J. Comput. Phys., 160, 405.
Barabási, A.L., & Stanley, H.E. 1995, *Fractal Concepts in Surface Growth*, (Cambridge Univ. Press)
Berera, A., & Fang, L.-Z. 1994, Phys. Rev. Lett., 72, 458

Bi, H.G. 1993, *ApJ*, 405, 479

Bi, H.G., Börner, G., & Chu, Y.Q. 1992, *A&A*, 266, 1

Bi, H.G., & Davidsen, A. F. 1997, *ApJ*, 479, 523

Bi, H.G., & Fang, L.Z. 1996, *ApJ*, 466, 614

Borgani, S., Governato, F., Wadsley, J., Menci, N., Tozzi, P., Quinn, T., Stadel, J., & Lake, G. 2002, *MNRAS*, 336, 409

Borve, S., Omang, M., & Trulsen, J. 2001, *ApJ*, 561, 82

Buchert, T., Domínguez, A., & Pérez-Mercader, J. 1999, *A&A*, 349, 343

Carrillo, J.A., Gamba, I.M., Majorana, A., & Shu, C.-W. 2003, *J. Comput. Phys.*, 184, 498

Cavaliere, A., Menci, N., & Tozzi, P. 1998, *ApJ*, 501, 493

Cen, R. 1992, *ApJS*, 78, 341

Cen, R., & Ostriker, J. 1999, *ApJ*, 514, 1

Cole, S., Aragon-Salamanca, A., Frenk, C., Navarro, J., & Zepf, S. 1994, *MNRAS*, 271, 781

Coles, P., & Spencer, K. 2003, *MNRAS*, 342, 176

Collella, P. & Woodward, P.R. 1984, *J. of Comp. Phys.* 54, 174

Davé, R., Cen, R., Ostriker, J., Bryan, G.L., Hernquist, L., Katz, N., Weinberg, D.H., Norman, M.L., & O’Shea, B. 2001, *ApJ*, 552, 473

Del Zanna, L., Velli, M., & Londrillo, P. 1998, *A&A*, 330, L13

Efstathiou, G., 1992, *MNRAS*, 256, 43

Eisenstein, D., & Hu, W. 1998, *ApJ*, 496, 605

Fang, L.Z., Bi, H.G., Xiang, S.P., & Börner, G. 1993, *ApJ*, 413, 477

Fedkiw, R.P., Sapiro, G., & Shu, C.W. 2003, *J. Comput. Phys.*, 185, 309

Feng, L.L., Pando, J., & Fang, L.Z. 2003, *ApJ*, 587, 487

Feng, L.L., Shu, C.W., & Zhang, M.P. 2004, *ApJ*, 612, 1

Gnedin, N.Y., & Hui, L. 1998, *MNRAS*, 296, 44

Gnedin, N.Y. 2000, *ApJ*, 542, 535

Godlewski, E., & Raviart, P.A. 1996, Numerical approximation of hyperbolic systems of conservation laws, (Springer)

Grasso, F., & Pirozzoli, S. 2000a, *Theor. Comp. Fluid Dyn.*, 13, 421

Grasso, F., & Pirozzoli, S. 2000b, *Phys. Fluids*, 12, 205

Harten, A. 1983, J. of Comp. Phys. 49, 357

Harten, A., Osher, S., Engquist, B., & Chakravarthy, S. 1986, Applied Numerical Mathematics, 2, 347

Hui, L., & Gnedin, N.Y., 1997, MNRAS, 292, 27

Jamkhedkar, P., Feng, L.L., Zheng, W., Kirkman, D., Tytler, D., & Fang, L.Z. 2003, MNRAS, 343, 1110

Jamkhedkar, P., Zhan, H., & Fang, L.Z. 2000, ApJ, 543, L1

Jiang, G., & Shu, C.W. 1996, J. Comput. Phys., 126, 202

Jiang, G., & Wu, C.C. 1999, J. Comput. Phys., 150, 561

Jones, B.T., 1999, MNRAS, 307, 376

Kaiser, N. 1986, MNRAS, 222, 323

Kardar, M., Parisi, G., & Zhang, Y.C. 1986, Phys. Rev. Lett., 56, 889

Katz, N., Weinberg, D.H., & Hernquist, L. 1996, ApJS, 105, 19

Kay, S. & Bower, R. 1999, MNRAS, 308, 664

Kraichnan, R.H. 1968, Phys. Rev., 174, 240

Kraichnan, R.H. 1994, Phys. Rev. Lett., 72, 1016

Landau, L., & Lifshitz, E. 1959, Fluid Mechanics, (Pergamon Press)

Lässig, M. 2000, Phys. Rev. Lett., 84, 2618

Liang, S., & Chen, H., 1999, AIAA J., 37, 1010

Liu, X.-D, Osher, S. & Chan, T. 1994, J. Comput. Phys., 115, 200

Lloyd-Davies, E., Ponman, T., & Cannon, D. 2000, MNRAS, 315, 689

Ma, C.P., & Bertschinger, E. 2004, ApJ, in press (astro-ph/0311049)

Matarrese, S., & Mohayaee, R. 2002, MNRAS, 329, 37

Mo, H.J., & Mao, S.D. 2002, MNRAS, 333, 768

Nakao, H. 1998, Phys. Rev. E, 58, 1591

Nusser, A. 2000, MNRAS, 317, 902

Nusser, A., & Haehnelt, M. 1999, MNRAS, 303, 179

Omang, M., Borve, S., & Trulsen, J. 2003, Comput. Fluid Dynamics, 12, 32.

Pando, J., Feng, L.L., Jamkhedkar, P., Zheng, W., Kirkman, D., Tytler, D., & Fang, L. Z. 2002, ApJ, 574, 575

Ponman, T., Cannon, D., & Navarro, J. 1999, *Nature*, 397, 135

Ponman, T., Sanderson, A., & Finoguenov, A. 2003, *MNRAS*, 343, 331

Ryu, D., Kang, H., Hallman, E., & Jones, T.W. 2003, *ApJ*, 593, 599

Ryu, D., Ostriker, O., Kang, H., & Cen, R. 1993, *ApJ*, 414, 1

Shandarin, S.F., & Zel'dovich, Ya.B. 1989, *Rev. Mod. Phys.*, 61, 185

Shi, J., Zhang, Y.T., & Shu, C.W. 2003, *J. Comput. Phys.*, 186, 690

Shraiman B.I., & Siggia, E.D. 2000, *Nature*, 405, 639

Shu, C.W. 1998, in *Advanced Numerical Approximation of Nonlinear Hyperbolic Equations*, Ed. A. Quarteroni, *Lecture Notes in Mathematics*, (Springer), 1697, 325

Shu, C.W. 1999, in *High-Order Methods for Computational Physics*, Eds. T.J. Barth and H. Deconinck, *Lecture Notes in Computational Science and Engineering*, (Springer), volume 9, 439

Shu, C.W. 2003, *Int. J. Comput. Fluid Dyn.*, 17, 107

Somerville, R.S., & Primack, J.R. 1999, *MNRAS*, 310, 1087

Springel, V., & Hernquist, L. 2002, *MNRAS*, 333, 649

Theuns, T., Leonard, A., Efstathiou, G., Pearce, F., & Thomas, P. 1998, *MNRAS*, 301, 478

Theuns, T., Schaye, J., Haehnelt, M., 2000, *MNRAS*, 315, 600

Valageas, P., Schaeffer, R., & Silk, J. 2002, *A&A*, 388, 741

Valageas, P., Schaeffer, R., & Silk, J. 2003, *MNRAS*, 344, 53 (VSS03)

Walker, T.P., Steigman, G., Kang, H.S., Schramm, D.M., & Olive K.A. 1991, *ApJ*, 376, 51

Xu, W., Fang, L.Z., & Wu, X.P. 1998, *ApJ*, 508, 472

Zhan, H. & Fang, L.Z., 2002, *ApJ*, 566, 9

Zhang, Y.T., Shi, J., Shu, C.W., & Zhou, Y. 2003, *Phys. Rev. E* 68, 046709

Fig. 1.— One-dimensional spatial distributions of temperature T , mass density ρ_{igm} , and velocity of the IGM (solid lines), and mass density ρ_{dm} and v_{dm} of dark matter (dashed lines) at $z=0$ and 0.5. The densities ρ_{dm} and ρ_{igm} are in units of $\bar{\rho}_{dm}$ and $\bar{\rho}_{igm}$, which are the mean densities of dark matter and gas, respectively.

Fig. 2.— Temperature T vs. IGM density ρ_{igm} . Each panel is given by 19,200 points randomly drawn from the simulation sample in $25^3 h^{-3} \text{ Mpc}^3$ box with 192^3 data points.

Fig. 3.— Relations of the mean baryon fraction with respect to temperature of the IGM. The redshifts are taken to be 4.0, 2.0, 1.0, and 0.

Fig. 4.— Relations of the cumulated probability of WHIM ($T > 10^5 \text{ K}$) with respect to the dark matter density ρ_{dm} . The redshifts are taken to be 4.0, 2.0, 1.0, and 0.

Fig. 5.— PDFs of the IGM temperature field in the ranges of $0.1 < \rho_{dm} < 0.4$, $0.4 < \rho_{dm} < 2$, and $2 < \rho_{dm} < 10$, respectively. The redshifts are taken to be 4.0, 2.0, 1.0, and 0.

Fig. 6.— Mean temperature \bar{T} vs. ρ_{dm} for samples smoothed on scales $L_J = 0.26, 1.04$, and $4.17 \text{ h}^{-1} \text{ Mpc}$, respectively. The redshifts are taken to be 4.0, 2.0, 1.0, and 0.

Fig. 7.— Entropy S vs. Temperature T . Each panel is given by 19,200 points randomly drawn from the simulation sample in a $25^3 h^{-3} \text{ Mpc}^3$ box with 192^3 data points.

Fig. 8.— Entropy S vs. dark matter density ρ_{dm} . Each panel is given by 19,200 points randomly drawn from the simulation sample in a $25^3 h^{-3} \text{ Mpc}^3$ box with 192^3 data points.

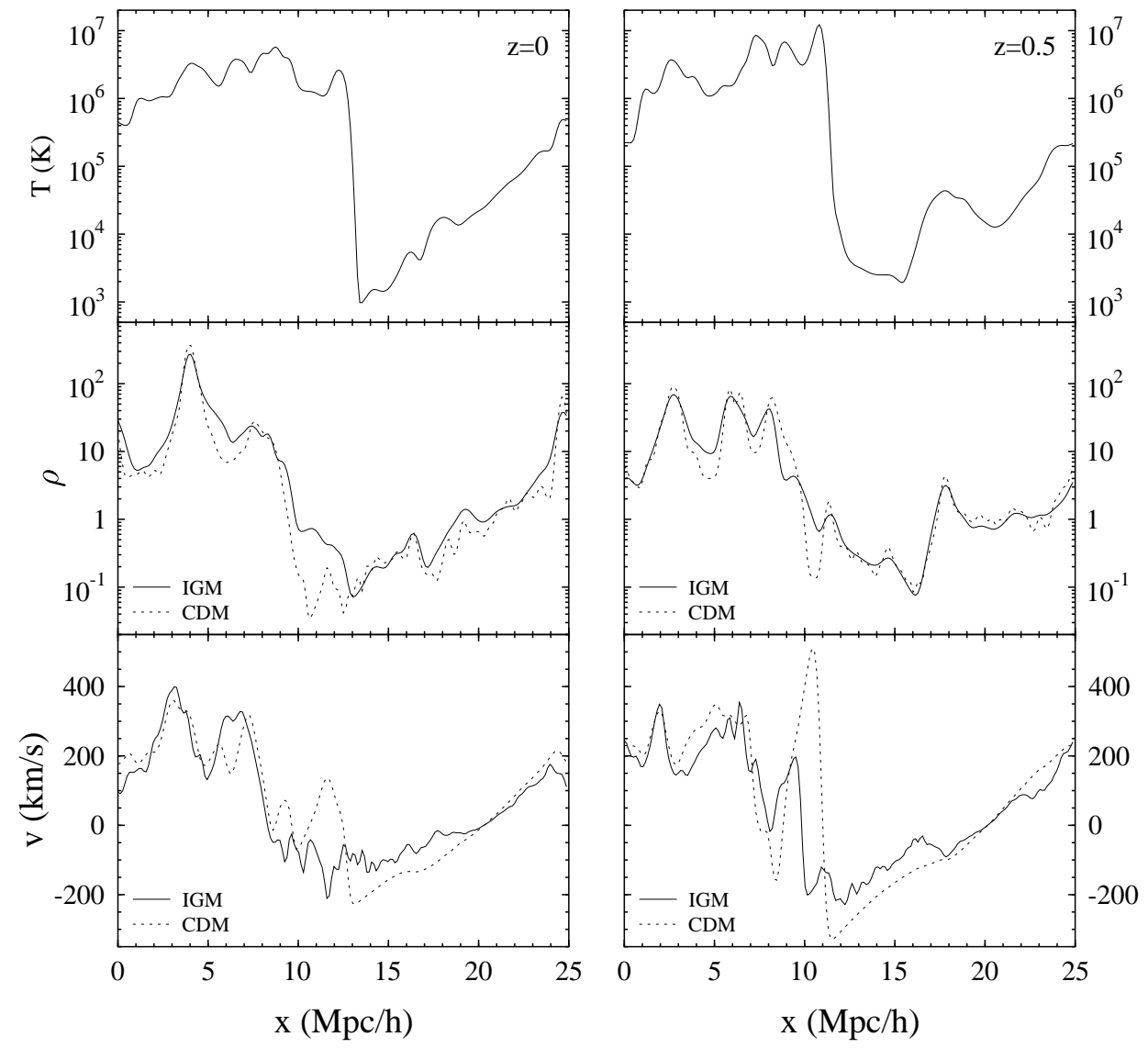
Fig. 9.— Mean entropy \bar{S} vs. ρ_{dm} (a) for the simulation with ionizing, radiation heating, and cooling at redshifts 4.0, 3.0, 2.0, 1.0, 0.5, and 0.0, and (b) for the simulation without ionizing, radiation heating, and cooling at redshifts 4.0, 2.0, 0.5, and 0.0.

Fig. 10.— PDFs of entropy field at redshifts 4.0, 3.0, 2.0, 1.0, 0.5, and 0.0, respectively.

Fig. 11.— Volume filling factors of entropy S field at redshifts 4.0, 3.0, 2.0, 1.0, 0.5, and 0.0, respectively.

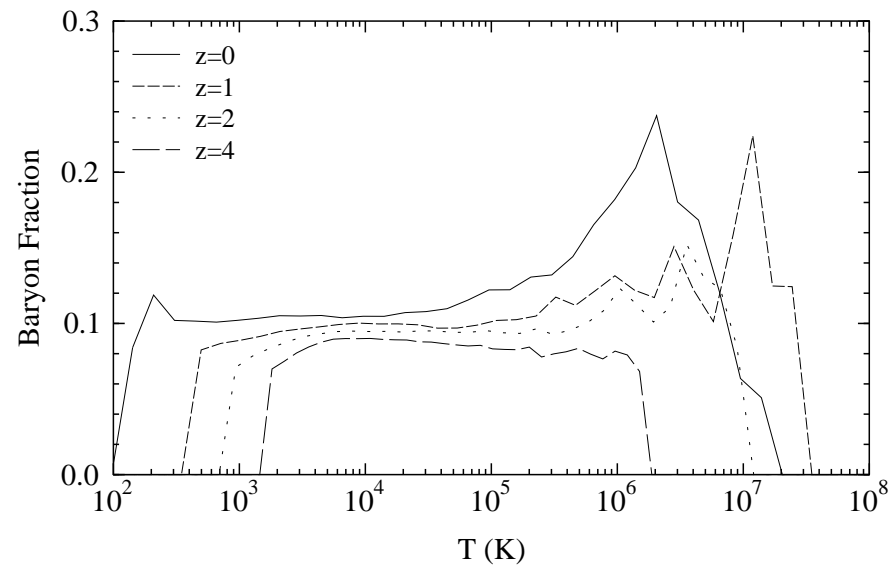
Fig. 12.— Baryonic mass fraction with entropy larger than 10, 50, 100, 200, 500, and 1000 $h^{-1/3} \text{ keV cm}^2$, and ρ_{dm} larger than 5(left panel) and 10 (right panel), respectively.

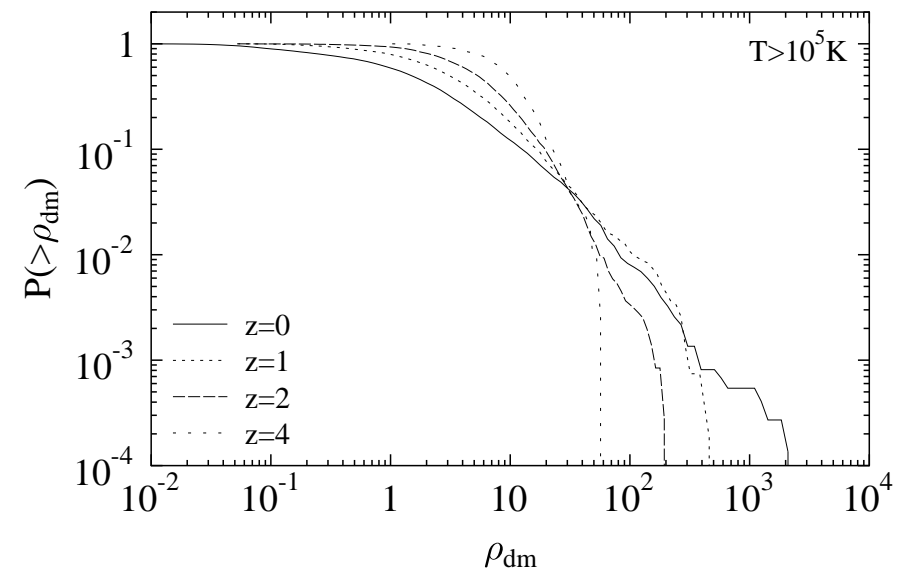
Fig. 13.— Mean entropy \bar{S} vs. ρ_{dm} for samples smoothed on scales $L_J = 0.26, 1.04$, and $4.17 \text{ h}^{-1} \text{ Mpc}$. The redshifts are taken to be 4.0, 3.0, 2.0, 1.0, 0.5, and 0.

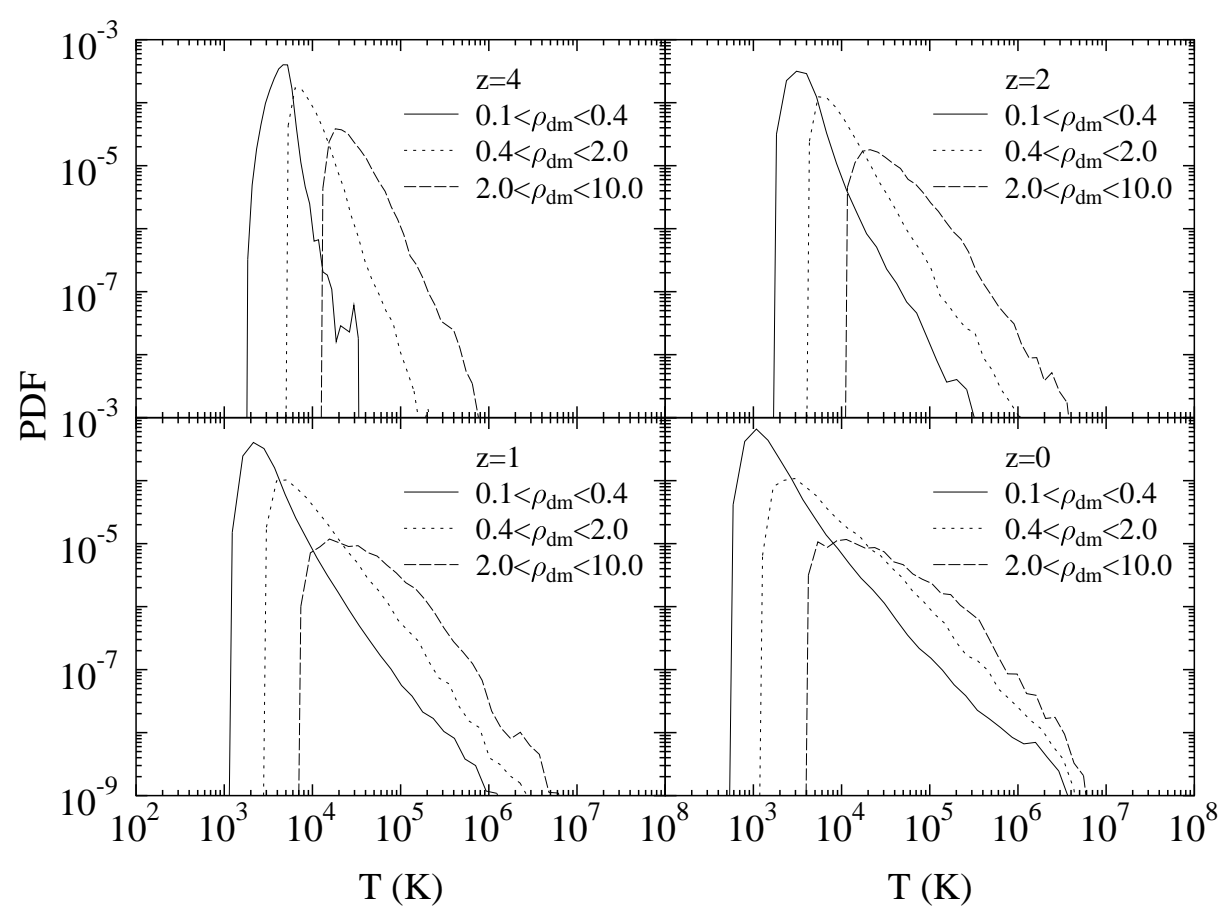


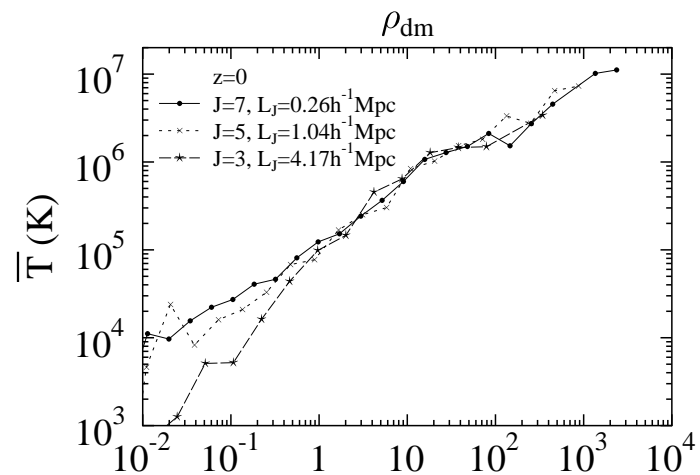
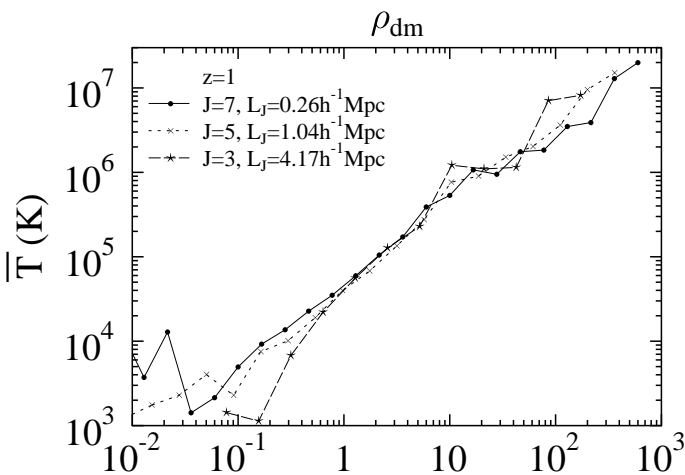
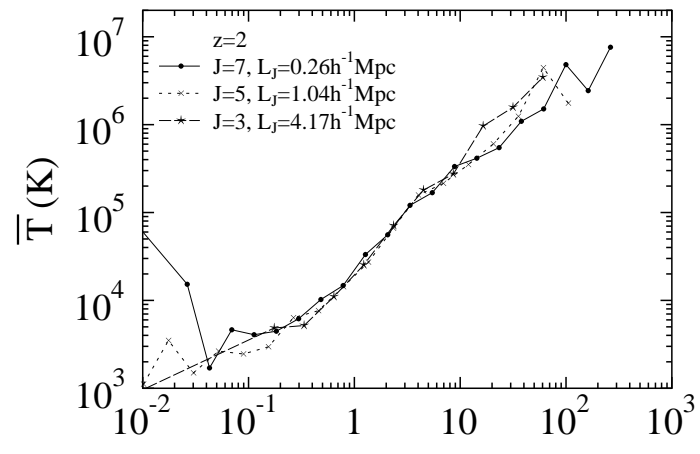
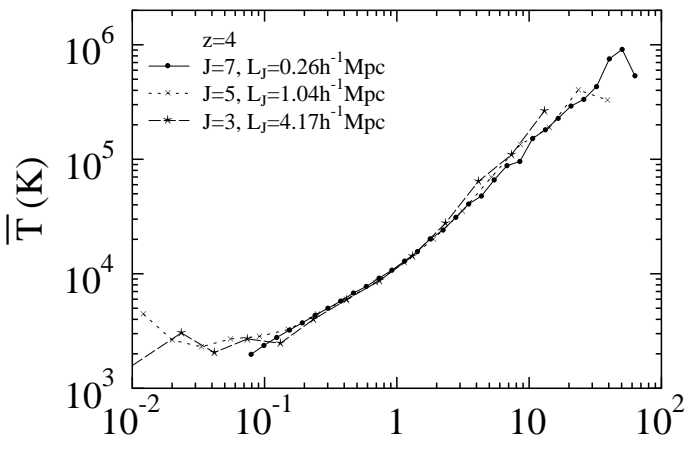
This figure "fig2.jpg" is available in "jpg" format from:

<http://arxiv.org/ps/astro-ph/0405139v2>







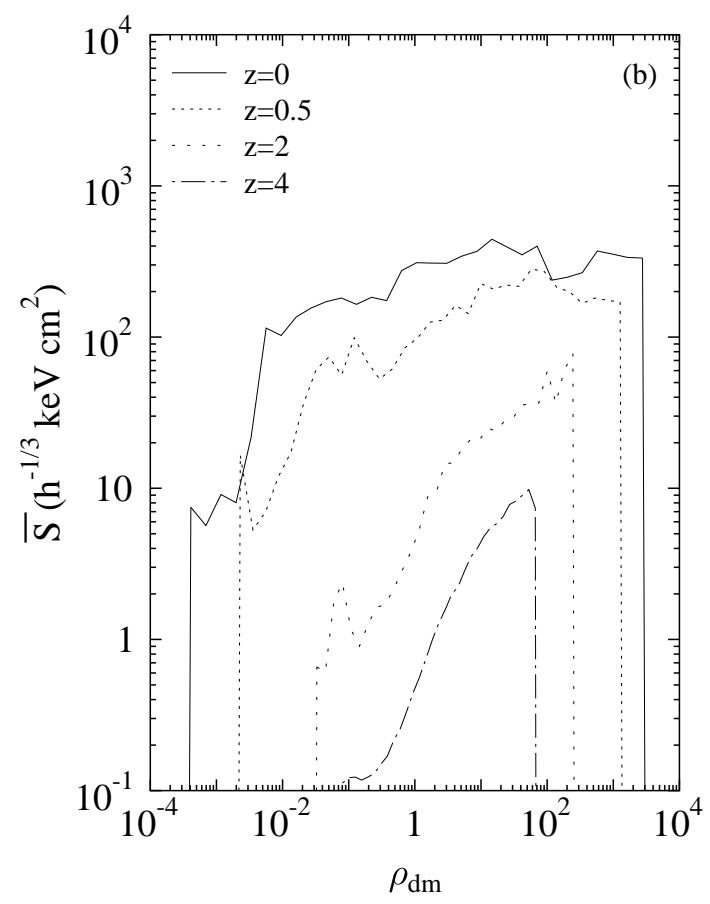
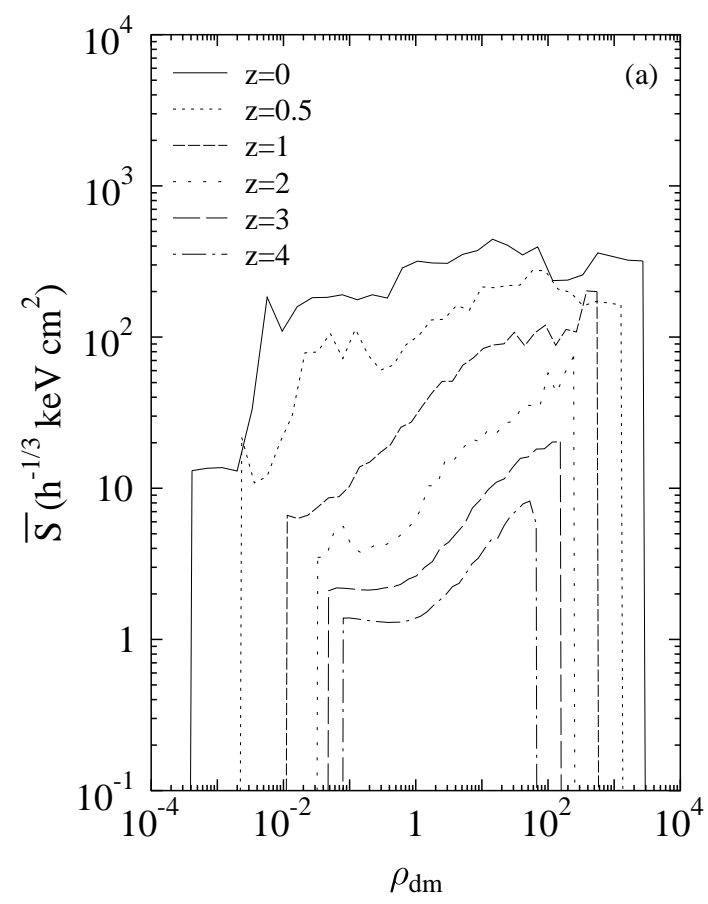


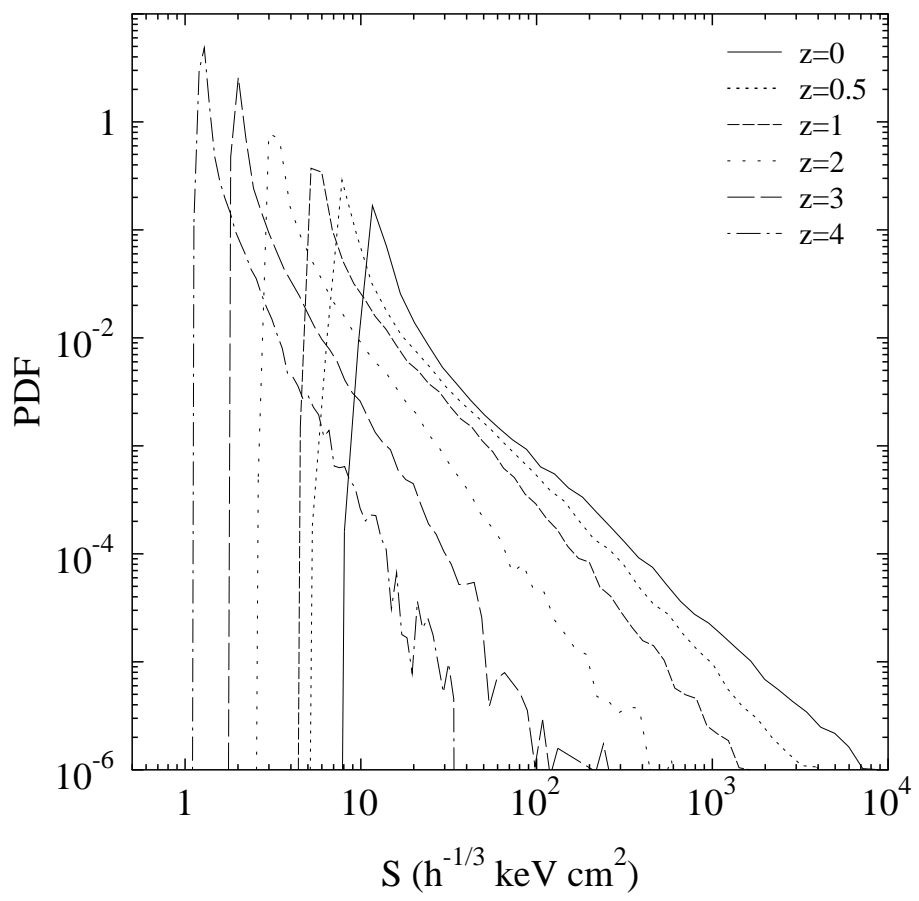
This figure "fig7.jpg" is available in "jpg" format from:

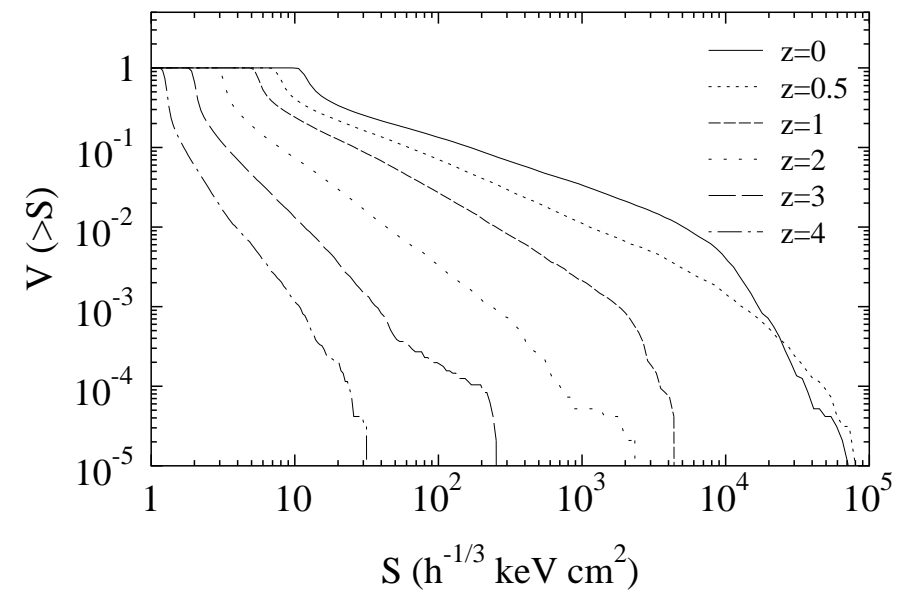
<http://arxiv.org/ps/astro-ph/0405139v2>

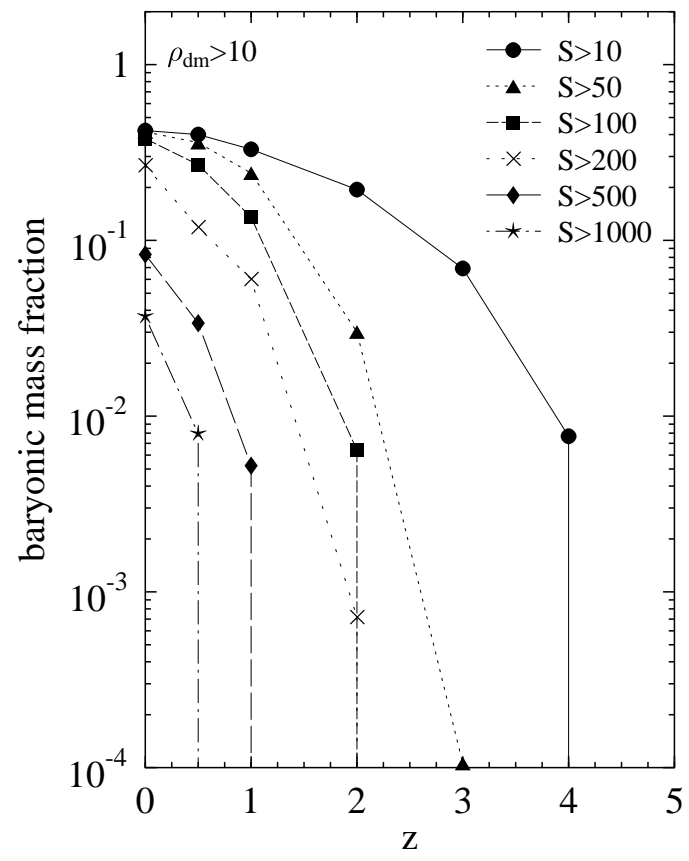
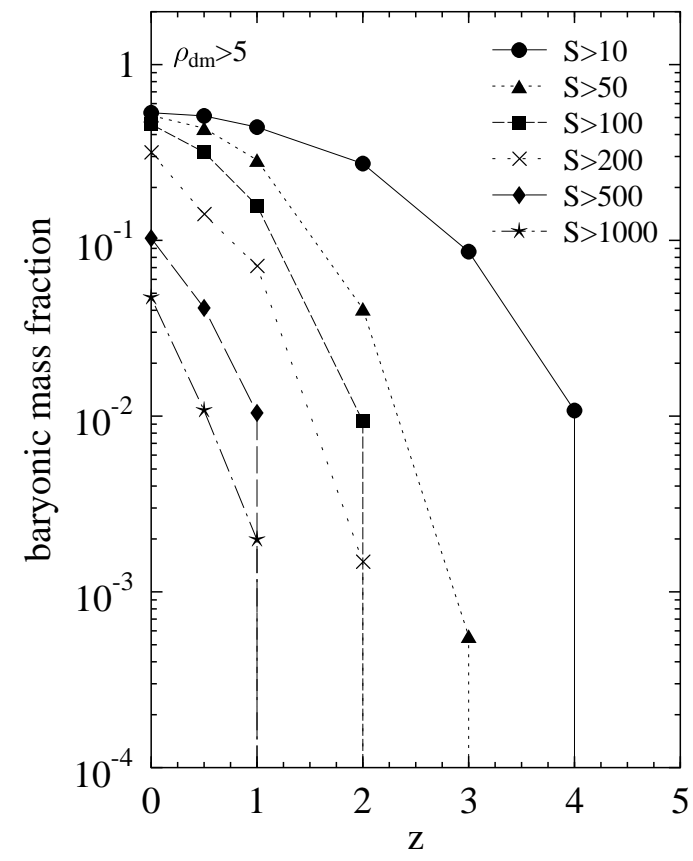
This figure "fig8.jpg" is available in "jpg" format from:

<http://arxiv.org/ps/astro-ph/0405139v2>









This figure "fig13.jpg" is available in "jpg" format from:

<http://arxiv.org/ps/astro-ph/0405139v2>